Minerals Engineering 239 (2026) 110115

Contents lists available at ScienceDirect

Minerals Engineering

journal homepage: www.elsevier.com/locate/mineng

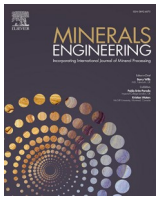

Early-stage temperature-dependent leaching kinetics and mechanisms of saprolitic and limonitic nickel laterite ores under atmospheric conditions

Heewon Kang, Jeongwoo Kim, Jaehoon Lee, Dagyeong Lee, Daniel Ko, Hyunjung Kim *

Department of Earth Resources and Environmental Engineering, Hanyang University, 222 Wangsimni-ro, Seongdong-gu, Seoul 04763, South Korea

ARTICLE INFO

Keywords:
Nickel laterite ore
Saprolitic ore
Limonitic ore
Leaching
Kinetics
Temperature

ABSTRACT

This study investigates the early-stage leaching behavior and temperature-dependent kinetics of saprolitic laterite (SL) and limonitic laterite (LL) ores under atmospheric acid leaching conditions at various temperatures to capture early-stage dissolution of nickel, magnesium, and iron. Both ores exhibited temperature-dependent increases in metal extraction, with highest extractions observed at 45 °C for saprolitic laterite ore and 65 °C for limonitic laterite ore. Structural analysis of leach residues revealed that the highest extractions corresponded to progressive collapse of key minerals—lizardite in saprolitic laterite ore and goethite and clinochlore in limonitic laterite ore. Kinetic analysis using a shrinking core model showed that solid product layer diffusion was the dominant rate-limiting step for all metals in both ores. Activation energies exceeding 56 kJ/mol for all metals suggested diffusion resistances, likely due to the formation of silica-rich product layers. This study clarifies the mineral leach mechanisms governing early-stage leaching in saprolitic laterite and limonitic laterite ores and provide a basis for optimizing selective nickel leaching.

1. Introduction

Over three million tons of nickel are produced and used annually globally, primarily due to growing demand for electric vehicles (EVs) (IEA, 2024a). Nickel is an essential component in various lithium-ion battery types, which offer high energy density and long cycle life (Tabrizi et al., 2024; Wu et al., 2024). EV battery demand increased by 40% in 2023 compared to 2022, surpassing 750 GWh, with 95% of this growth attributed to rising EV sales (IEA, 2024b). Nickel demand for batteries alone reached nearly 370 kt—approximately 30% higher than in 2022, accounting for over 10% of total nickel demand (IEA, 2024b). Therefore, there is an urgent need to secure nickel resources (IEA, 2024a). Nickel resources are broadly divided into nickel sulfide ore and nickel laterite ore, with the latter further classified into saprolitic laterite (SL) and limonitic laterite (LL) ores (Mweene et al., 2024a). Although nickel sulfide ore has historically been preferred due to its amenability to conventional smelting and refining, the increasing demand for nickel has led to an expansion of nickel laterite ore development (Mudd, 2009; Zhang et al., 2024). LL ore, which contains nickel and iron as oxides, is typically treated through high-pressure acid leaching, but high temperature, pressure, and acid consumption make this hydrometallurgical route less economical. In contrast, SL ore, rich in MgO, is processed via energy-intensive pyrometallurgical routes to circumvent high acid consumption (Pandey et al., 2023).

Atmospheric acid leaching (AAL) has been increasingly adopted owing to its low operational cost, ambient-pressure conditions, and moderate temperatures (<100 °C) (Li et al., 2013). Consequently, research has been conducted to optimize nickel leaching in nickel laterite ore using AAL (Karppinen et al., 2024; MacCarthy et al., 2016; McDonald and Whittington, 2008; Thubakgale et al., 2013; Tunç Parlak and Yildiz, 2024). MacCarthy et al. investigated sulfuric acid leaching under atmospheric conditions and demonstrated that nickel extraction increased with changes in operational parameters such as temperature and leaching time (MacCarthy et al., 2016). They also suggested that the enhanced dissolution of iron and magnesium can substantially increase acid consumption, thereby reducing overall process efficiency. In addition, Astuti et al. conducted atmospheric leaching of Indonesian saprolitic ores using citric acid and reported that nickel dissolution responses differed among ores even under identical leaching conditions (Astuti et al., 2016).

The variability arises from the mineralogical characteristics of laterite ores, including ion substitution and structural resistance to acid attack (Faraji et al., 2022; Li et al., 2013; MacCarthy et al., 2016; Mweene et al., 2024b; Petrovski et al., 2019; Tunç Parlak and Yildiz,

* Corresponding author.
E-mail address: kshjkim@hanyang.ac.kr (H. Kim).

https://doi.org/10.1016/j.mineng.2026.110115
Received 24 November 2025; Received in revised form 17 January 2026; Accepted 23 January 2026
Available online 29 January 2026

2024). For example, ion substitution determines how nickel is hosted in minerals, thereby affecting its leachability. In LL ore, goethite is the dominant host of nickel, where nickel is often incorporated by substitution into the iron oxide lattice. During leaching, nickel release occurs via dissolution of the goethite structure, which is affected by the type of substituting ion (McDonald and Whittington, 2008). In SL ore, nickel often substitutes for magnesium in serpentine minerals, and the dissolution process involves the breakdown of weak Mg-O bonds following the removal of hydroxyl groups (Fan and Gerson, 2013; McDonald and Whittington, 2008). These mineral-specific behaviors suggest that leaching mechanisms and rate-controlling steps may differ between SL and LL ores.

A comparative kinetic analysis under controlled atmospheric conditions is essential to systematically understand these differences. Previous studies had focused on long-term dissolution trends and thus have not sufficiently addressed the structural collapse or metal-specific reactivity that occurs during the early stages of leaching (Jeong et al., 2025). Moreover, the substantial dissolution of iron and magnesium increases acid consumption and neutralizing agent demand, placing burdens on downstream purification processes. Understanding the early-stage dissolution rates and temperature responsiveness of nickel, magnesium, and iron is critical for designing selective leaching conditions. Yet the early stage, temperature-dependent mechanisms in SL and LL ores remain insufficiently resolved. This study investigates the temperature-dependent leaching kinetics of major metals in the early dissolution stage for two ore types under atmospheric conditions.

2. Materials and methods

2.1. Materials

A SL ore (~0.95 wt% Ni) from New Caledonia and a LL ore (~0.99 wt % Ni) from the Philippines were used. Ore samples were dried at 80 °C in an oven for 24 h and ground using a ball mill under 100 mesh for subsequent ore characterization and leaching experiments. Mineralogical analyses were conducted using (i) X-ray fluorescence spectrometry (XRF, ZSX Primus IV, Rigaku, Japan), (ii) Fourier transform infrared spectroscopy (FTIR, Nicolet iS50, Thermo Scientific, USA) (64 scans recorded in the scanning range of 4000–400 cm^{-1} with a resolution of 1 cm^{-1}), and (iii) X-ray diffractometry (XRD, D8 Advance, Bruker, Germany) (Cu-Kα wavelength of 1.5418 Å, scanning range of 5°-90°, and a scan speed time of 0.4 s) with the DIFFRAC.EVA software (Bruker, Germany). For each sample, 3 g of subsamples were dissolved in aqua regia (HCl:HNO_3 = 3:1) at 25 °C for 2 h and then digested at 150 °C for another 2 h. The digested subsamples were analyzed using inductively coupled plasma atomic emission spectroscopy (ICP-OES, iCAP 7400 Duo, Thermo Scientific, USA) to obtain their chemical composition.

2.2. Batch leaching experiments

Leaching experiments were conducted in batches at various temperatures to study nickel (Ni), magnesium (Mg), and iron (Fe) leaching from SL and LL ores. Sulfuric acid (H_2SO_4, 98% purity, Sigma-Aldrich) was used as the leaching agent. A total of 40 mL of the leaching agent diluted to 400 kg H_2SO_4/dmt (acid weight per dry metric ton of ore; corresponding to an initial sulfuric acid concentration of ~ 0.5 mol/L; pulp density was 125 g/L) was added to a 100 mL beaker, and then stirred at a constant speed of 300 rpm using a magnetic stirrer. For each sample, 5 g of solids were added to the leaching agent after the desired temperature was reached. The temperature was adjusted using a hotplate. Additionally, a watch glass was placed over the beaker to minimize evaporation. For SL ore, leaching temperatures were 25 °C, 35 °C, and 45 °C with leaching times of 2–60 min for each temperature. For LL ore, leaching temperatures were 25 °C, 45 °C, and 65 °C with leaching times of 5–480 min for each temperature. The difference in temperature and time ranges reflects the distinct mineralogical characteristics and reactivity of the two ore types (Jeong et al., 2025; Rubisov et al., 2000).

To evaluate potential mixing limitations, additional leaching tests were conducted at different agitation speeds (200–500 rpm) at the highest leaching temperature for each ore. All other experimental parameters (acid dosage and pulp density) were kept identical to those used in the standard leaching experiments. For SL ore, under 200 mesh fraction was used in the agitation-speed tests due to sample availability, whereas the LL ore was tested using the same size fraction as in the baseline experiments.

After leaching, solid–liquid separation was conducted by filtration with a 0.2 μm syringe filter. The liquid phase was analyzed using titration (905 titrando, Metrohm, Switzerland) (program Tiamo 2.5) to calculate the acid consumption (Eq. (1)) by titrimetric methods (Li et al., 2013; Rolia and Dutrizac, 1984; Srinivasan and Rao, 2014; von Barsewisch and Hasty, 1985), and ICP-OES to calculate the metal leaching efficiency (Eq. (2)).

$$\text{Acid consumption}\ (\text{kg}\,H_2SO_4/\text{dmt}) = \frac{(A_i - A_f)\,V M_{H_2SO_4}}{m_{ore}} \times 1000 \quad (1)$$

$$\text{Leaching efficiency}\ (\%) = \frac{M_f}{M_i} \times 100 \quad (2)$$

where A_i and A_f are the initial and final sulfuric acid concentrations (mol/L), V the solution volume (L), M_{H2SO4} the molar mass of sulfuric acid (98.08 g/mol), m_{ore} the dry ore mass (g), and M_i and M_f are the metal masses in the ore and leachate (mg), respectively.

The leached residues were washed with deionized (DI) water (Milli-Q water), dried at 80 °C for 1 d, ground, and analyzed with XRD and FTIR to investigate the leaching mechanism. To minimize the influence of surface-adsorbed sulfate species on FTIR interpretation, leach residues were additionally washed with a phosphate buffer solution (0.05 mol/L, pH 7), followed by thorough rinsing with DI water, and the dried and ground prior to FTIR analysis (Ganta et al., 2021); the resulting spectra were compared with those obtained from deionized water washed residues.

2.3. Kinetic analysis method

The acid leaching of nickel laterite ore can be explained by the shrinking core (SC) model (Faraji et al., 2022; Li et al., 2019; Wanta et al., 2016), in which the solid particle maintains its bulk size while the unreacted core gradually shrinks throughout leaching, forming a product layer around it (MacCarthy et al., 2016). In the solid–liquid system of the SC model, the leaching reaction is controlled by one of three mechanisms: (i) liquid film diffusion (diffusion through the liquid film formed around the solid particle), (ii) solid product layer diffusion (diffusion through the solid product layer surrounding the unreacted core), and (iii) chemical reaction (chemical reaction at the surface of the unreacted core) (Gharabaghi et al., 2013; MacCarthy et al., 2016). The three rate-limiting mechanisms in the SC model and their activation energy (E_a) in the Arrhenius equation were expressed as:

$$X = k_f t \quad (3)$$

$$1 - 3(1-X)^{2/3} + 2(1-X) = k_p t \quad (4)$$

$$1 - (1-X)^{1/3} = k_r t \quad (5)$$

$$k = A e^{-E_a/RT} \quad (6)$$

where X is the reacted fraction (dimensionless), t the leaching time (min), k_f (min^{-1}), k_p (min^{-1}), and k_r (min^{-1}) are the apparent rate constants of the three mechanisms, E_a the activation energy (J/mol), R the ideal gas constant (J/(mol K)), T the absolute temperature (K), A the frequency factor related to collision (min^{-1}), and k is leaching apparent rate constant (min^{-1}). The E_a was calculated from the slope of the

Table 1
Chemical composition (ICP-OES) and mineralogical composition (XRF) of the SL and LL ores.

	Elements (wt%)							Oxides (wt%)			Fe/Mg
	Ni	Fe	Mg	Co	Al	Cr	Mn	MgO	Fe_2O_3	SiO_2	
SL ore	0.95	11.87	14.44	0.07	0.24	0.15	0.19	30.28	17.57	32.60	0.82
LL ore	0.99	21.90	2.70	0.12	1.27	0.44	0.58	9.55	40.29	26.14	8.11

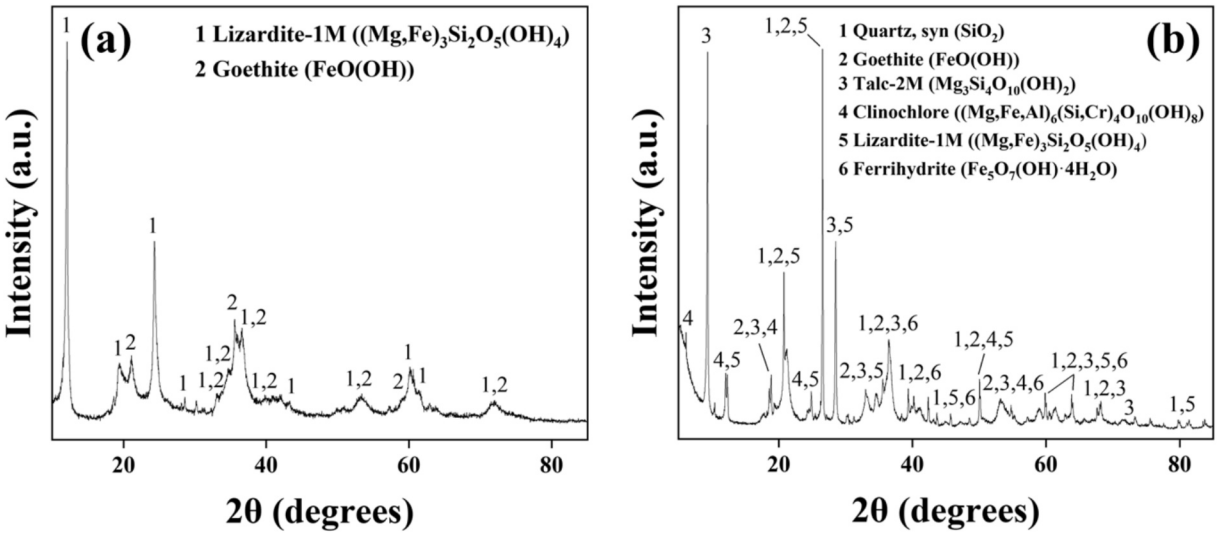

Fig. 1. XRD-based mineralogical profiles of the raw (a) SL and (b) LL ores.

Arrhenius plot of ln k versus $1/T$ (Eq. (6)), where the slope equals $-E_a/R$.

Akaike's information criterion (AIC) was employed to discriminate among the three SC models by accounting for goodness of fit. Model comparison was based on ΔAIC, defined as the difference between each model's AIC and the minimum AIC obtained for a given metal-temperature condition (ΔAIC = 0 for the model with the lowest AIC). The uncertainty of the activation energies derived from Arrhenius plots was additionally assessed using 95% confidence intervals (CI) of the regression slope. Model fitting and AIC calculations were performed in *Mathematica* 14.3 (Wolfram Research) using nonlinear regression, while 95% CI for activation energies were derived from Arrhenius regressions (slope CI).

Because the SC model assumes that the acid concentration in the bulk solution is spatially uniform and remains effectively constant during leaching, additional low-pulp density tests were conducted under excess-acid conditions (acid consumption remained below 10% of the initial acid) to verify whether the identified rate-limiting step remained unchanged. For both ores, 0.6 g sample was leached in 40 mL of 0.5 mol/L sulfuric acid (pulp density was 15 g/L), and the same kinetic analysis was applied. Tests were conducted at two representative temperatures for each ore (SL ore is 25 and 45 °C; LL ore is 25 and 65 °C), while agitation speed was kept 300 rpm. For SL ore, under 200 mesh fraction was used in the low-pulp density tests due to sample availability, whereas the LL ore was tested using the same size fraction as in the baseline experiments.

3. Results and discussion

3.1. Ore characterization

Table 1 shows that the Ni content was comparable in both ore samples, with Mg being the dominant component in SL ore (Fe/Mg = 0.82) and Fe in LL ore (Fe/Mg = 8.11), which is consistent with previous studies (Fan et al., 2024; Liu et al., 2024; Mweene et al., 2024a; Urtnasan et al., 2025). The Fe/Mg ratio serves as a simple indicator of Mg-rich (saprolitic) and Fe-rich (limonitic) laterite characteristics. Fig. 1a shows that lizardite (PDF 00-050-1606) was the major mineral in SL ore, while goethite (PDF 00-029-0713) was the minor mineral. Fig. 1b shows that goethite (PDF 00-029-0713) and talc (PDF 00-029-1493) exhibit the strongest reflections in LL ore, while quartz (PDF 00-046-1045), clinochlore (PDF 00-060-0313), lizardite (PDF 00-050-1606), and ferrihydrite (PDF 00-029-0712) were the minor minerals. However, based on the bulk chemical composition (Table 1), talc is limited to ≤ ~15 wt%, whereas Fe corresponds to ≥ ~35 wt% Fe-oxyhydroxides (e.g., goethite and ferrihydrite), indicating goethite dominance by mass. This confirmed that SL ore was indeed a saprolitic laterite ore and LL ore was a limonitic laterite ore.

3.2. Temperature-dependent leaching performance

Prior to discussing the temperature effect, agitation speed tests (200–500 rpm) were performed to assess potential mixing or external mass-transfer limitations. The leaching efficiencies of Mg, Ni, and Fe showed only minor variations with agitation speed for both SL and LL ores (Fig. S1), suggesting that the leaching behavior discussed below is not primarily governed by hydrodynamic conditions. Accordingly, 300 rpm was used for the temperature-dependent leaching tests.

Fig. 2 shows the results of the leaching experiments. Leaching rates of both SL and LL ores at the highest temperatures of 45 °C and 65 °C, respectively, were considerably higher than those at lower temperatures. For SL ore, Ni exhibited the highest leaching efficiency at all temperatures, followed by Mg and Fe (Fig. 2**a-c**). Notably, Mg leaching efficiency increased sharply at 45 °C, reaching 41%. For LL ore, Mg exhibited the highest leaching efficiency at all temperatures, reaching a final leaching efficiency of 80% at 65 °C, which was significantly higher than the 15% observed at 25 °C (Fig. 2**d-f**). The final leaching efficiency of Fe increased 13-fold (from 2% to 27%) as the temperature rose to 65 °C, indicating enhanced dissolution of Fe-bearing minerals at higher temperatures.

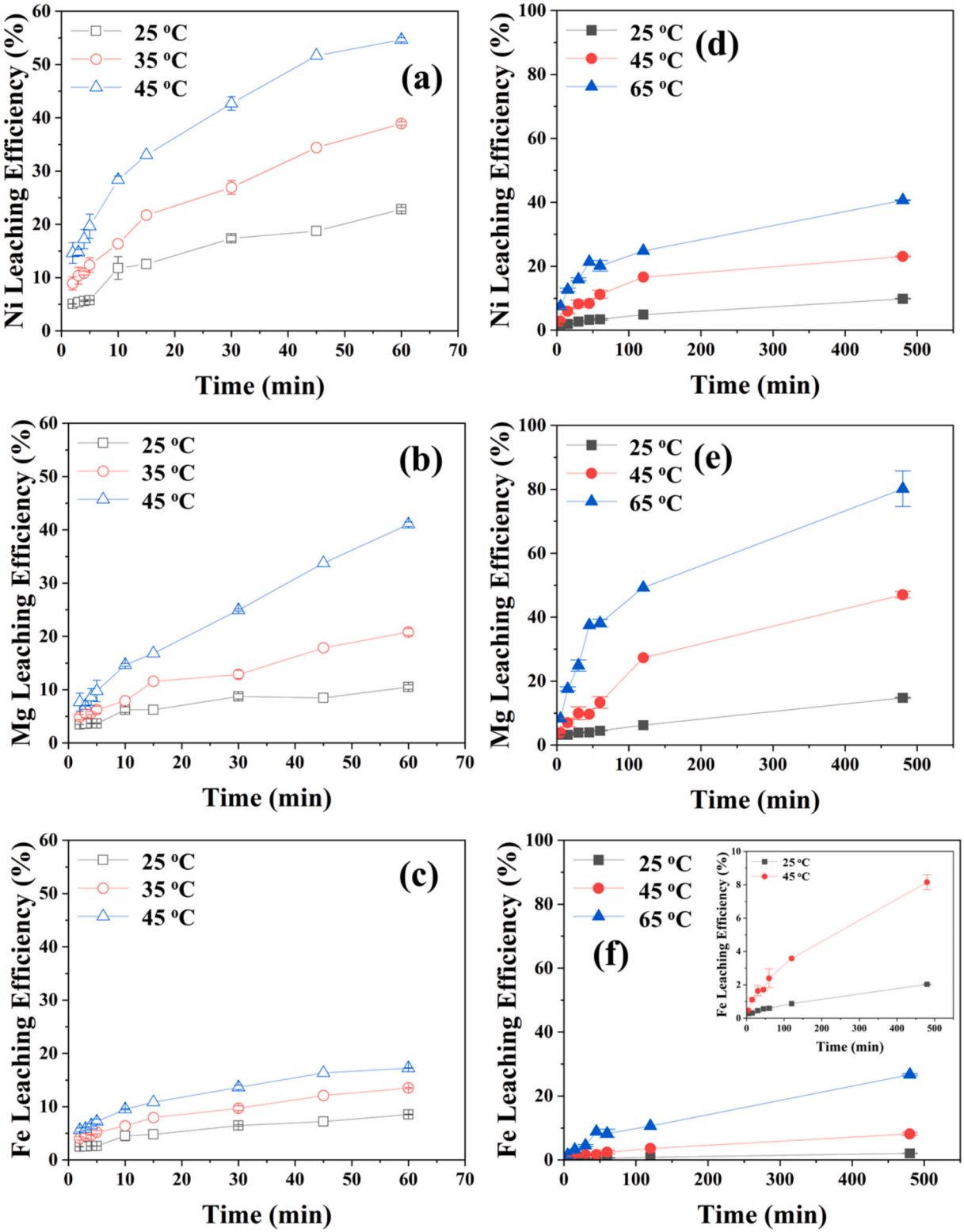

Fig. 2. Leaching efficiency of (a) Ni, (b) Mg, and (c) Fe of SL and (d) Ni, (e) Mg, and (f) Fe of LL ores as a function of time and temperature. The inset in (f) more clearly shows the leaching at 25 °C and 45 °C. The error bars represent standard deviation from replicate experiments ($n \leq 2$).

Fig. 3 shows the acid consumption of SL and LL ores at different temperatures. The corresponding numerical data are provided in Table S1. For SL ore, the highest acid consumption was observed at 45 °C, reaching 267 kg H_2SO_4/dmt at 60 min, which suggests that additional acid was consumed to facilitate the dissolution of refractory mineral phases at higher temperatures. However, LL ore had a lower acid consumption (94 kg H_2SO_4/dmt) than SL ore at 60 min despite the higher temperature (65 °C). Acid consumption continued to increase after 60 min at 65 °C, which is consistent with the sustained increase in Fe leaching efficiency over the prolonged leaching period (Fig. 2f). This suggests that Fe dissolution in LL ore persisted and led to additional acid consumption under high temperature conditions. The leaching

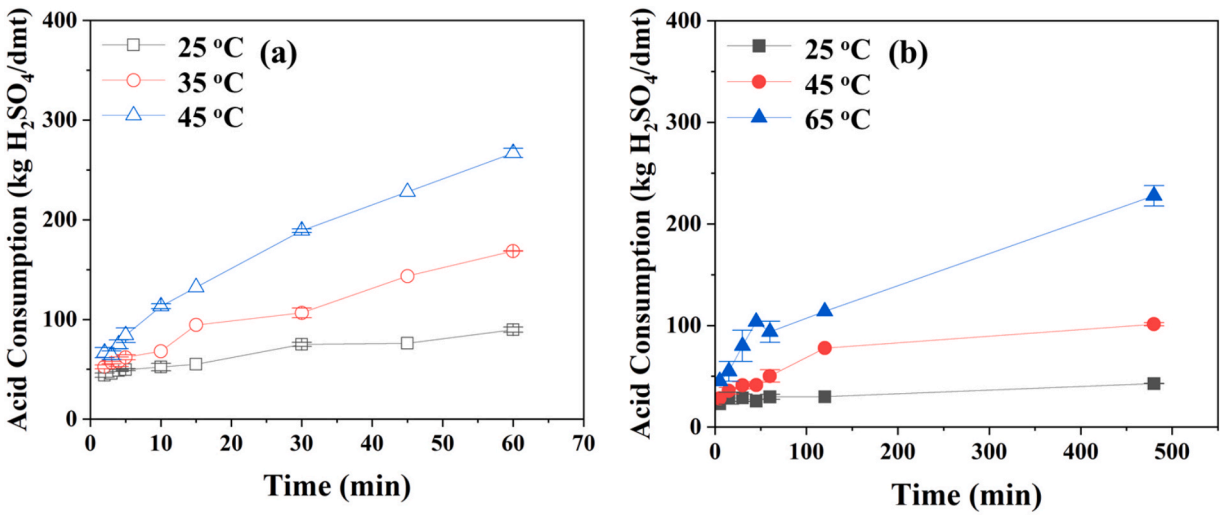

Fig. 3. Average acid consumption of (a) SL and (b) LL ores as a function of time and temperature. The error bars represent standard deviation from replicate experiments (n ≤ 2).

efficiency of Mg was higher than Fe for both ore types, which aligns with the preferential dissolution behavior of Mg-bearing lizardite, a phase structurally more susceptible to acid attack (Sufriadin et al., 2011).

3.3. Temperature-dependent dissolution behavior

3.3.1. Leaching mechanism

The XRD patterns of SL ore in Fig. 4**a-c** show a change in the intensity of the lizardite peak (2θ = 35°) within the first 30 min, indicating a progressive collapse of the lizardite structure over time. This early collapse behavior is consistent with findings from previous studies. Tian et al. reported that lizardite is more susceptible to acid attack than other silicates such as clinochlore, and consequently disappears first in the leach residues (Tian et al., 2021). This structural collapse was attributed to the susceptibility of its tetrahedral-octahedral (T-O) 1:1 layered structure to acid attack, which facilitates the preferential dissolution of Ni and Mg from the octahedral layer (Sufriadin et al., 2011). The FTIR spectra in Fig. 4**d-f** exhibit broadening of the peaks in the 1000–1500 cm^{-1} region, which is indicative of transformation to amorphous silica (Ellerbrock et al., 2022). Since the 1000–1200 cm^{-1} region can overlap with sulfate vibrations (Frost et al., 2015; Knittle et al., 2001), the residues were additionally washed with a phosphate buffer solution. The spectra remained unchanged relative to DI-washed residues (Fig. S2), supporting that the observed region is attributable to amorphous silica rather than sulfate species. In contrast, goethite exhibits minimal peak changes in both XRD and FTIR due to its thermally stable structure at low temperatures (Posnjak and Merwin, 1922).

Fig. 5**a-c** show the XRD patterns of LL ore leach residues. At 25 °C, only a minor peak (2θ = 70°) of lizardite was removed; however, at 45 °C and above, peaks associated with goethite, clinochlore, lizardite, and ferrihydrite partially decreased. This suggested that the structure of these minerals gradually broke down as the temperature increased. FTIR in Fig. 5**d-f** shows that the disappearance of the Al-O absorption peak at 3676 cm^{-1} after 480 min (Khattak et al., 2023; Tchio et al., 2024), indicating that a structural change occurred in clinochlore. In addition, at 65 °C, the Fe-O bonding vibration peak shifted from 621 cm^{-1} to 603 cm^{-1} (Kamwa et al., 2023; Khattak et al., 2023; Saadon et al., 2018), which was interpreted as an alteration of goethite due to partial dissolution (Chen et al., 1998). Talc and clinochlore have a tetrahedral-octahedral-tetrahedral (T-O-T) structure and therefore dissolve more slowly than lizardite (Sufriadin et al., 2011; Tian et al., 2021). Since ferrihydrite has an amorphous structure, it responds sensitively to temperature increases, leading to faster dissolution (Barrón et al., 2003; Norman, 2014).

3.3.2. Congruency of dissolution

Fig. 6 shows the correlation between Ni and other metals involved in its leaching behavior. Slope in Fig. 6 were obtained from linear regression, using separate fits for the initial and later leaching regimes. As a semi-quantitative indicator, a slope close to 1 indicates that Ni and another metal were leached in similar proportions, suggesting a high correlation between Ni and the metal. In contrast, a slope that deviates significantly from 1 suggests differing leaching behaviors between Ni and the metal, implying that Ni is distributed in different mineral phases (Landers and Gilkes, 2007).

For SL ore, the initial Ni-Mg slope was 0.51, indicating that Mg did not have a dominant influence on Ni leaching (Fig. 6a). However, the slope increased to 1.26 at 45 °C after 30 min, suggesting that Ni and Mg were co-dissolved as a result of the structural collapse of lizardite. The Ni-Fe slope remained low (0.34), implying that most of the dissolved Ni originated from Mg-bearing minerals. In Fig. 6b, for LL ore, the initial Ni-Mg slope was 1.29, indicating a high leaching correlation between the dissolution of Ni and Mg. As temperature increased, the slope further increased to 2.20 at 65 °C, suggesting accelerated dissolution of Mg-rich minerals (clinochlore or talc) and consequently pronounced Mg leaching. The Ni-Fe slope increased from 0.23 to 0.94, which attributed to enhanced dissolution of Fe-bearing minerals at higher temperatures, releasing Ni substituted in their structures.

3.4. Kinetic analysis

3.4.1. The shrinking core model fitting

To evaluate potential time-dependent changes in the rate-limiting mechanism, the leaching data were analyzed using two fitting approaches: (i) whole-time-range fitting over the entire leaching duration (Tables 2 and 3) and (ii) stage-wise fitting by dividing the curves into early and late intervals (SL ore, 0–5 and 5–60 min; LL ore, 0–30 and 30–480 min; Tables S2 and S3). For the stage-wise fitting, each interval was analyzed using the shifted form of the SC model equations, where conversion and time were referenced to the interval start point ($t - t_1$) and ($X - X_1$). The stage-wise fitting did not show a clear transition in the dominant rate-controlling step, and the resulting interpretation was generally consistent with the whole-time-range fitting. Accordingly, the kinetic discussion in the main text is based on the whole-time-range fitting results.

Based on the whole-time-range fitting, the leaching data of SL and LL

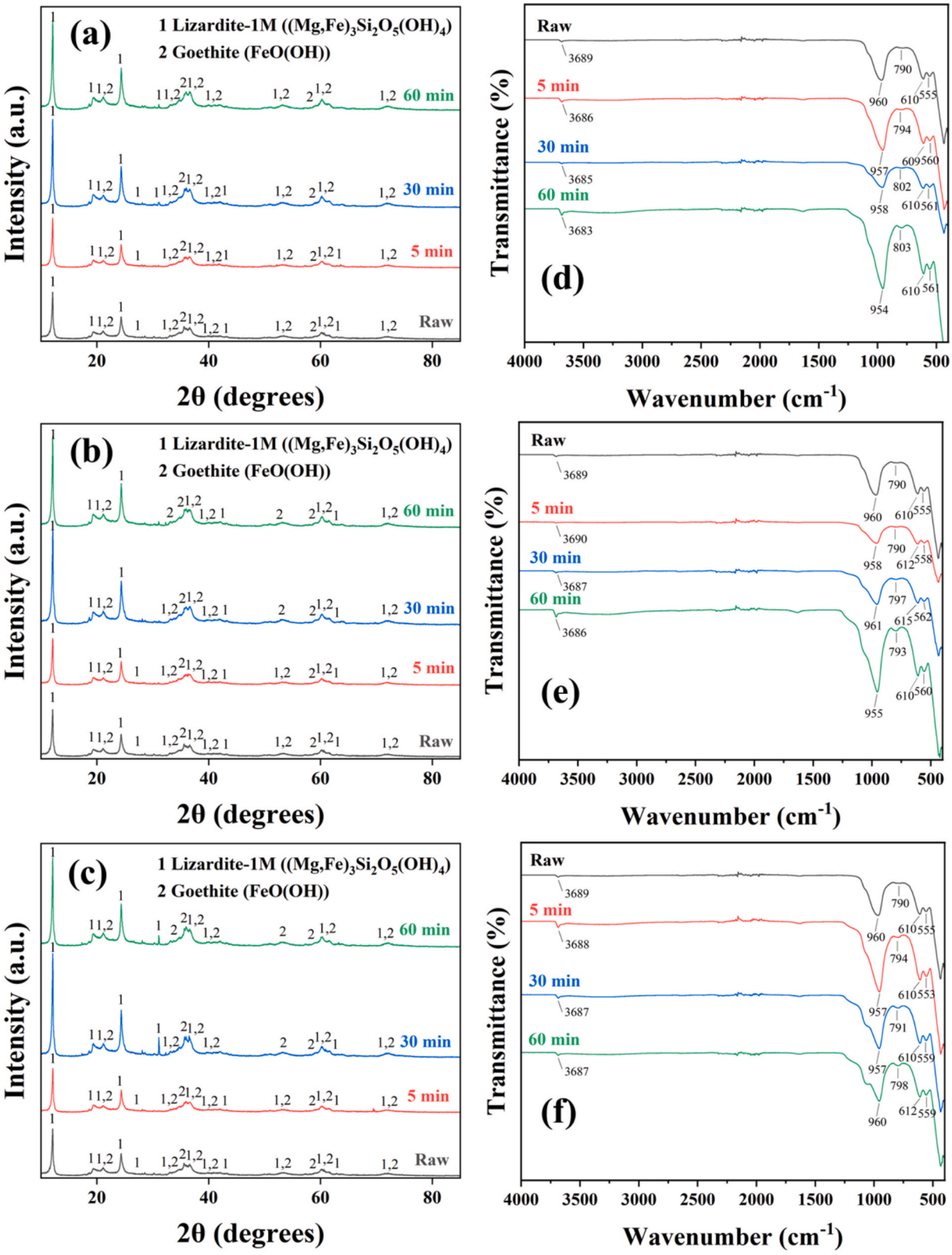

Fig. 4. X-ray diffraction patterns of SL ore leach residues at (a) 25 °C, (b) 35 °C, and (c) 45 °C, and corresponding Fourier-transform infrared spectra at (d) 25 °C, (e) 35 °C, and (f) 45 °C. Leaching times are shown in the legends.

ores were fitted to the SC models (Figs. S3 and S4) and the resulting apparent rate constants are summarized in Tables 2 and 3. Model discrimination was further evaluated using AIC (Tables S4 and S5). For both ores, the solid product layer diffusion control provided the best fit, indicated by the highest coefficient of determination (R^2) values and the lowest AIC values ($\Delta AIC = 0$).

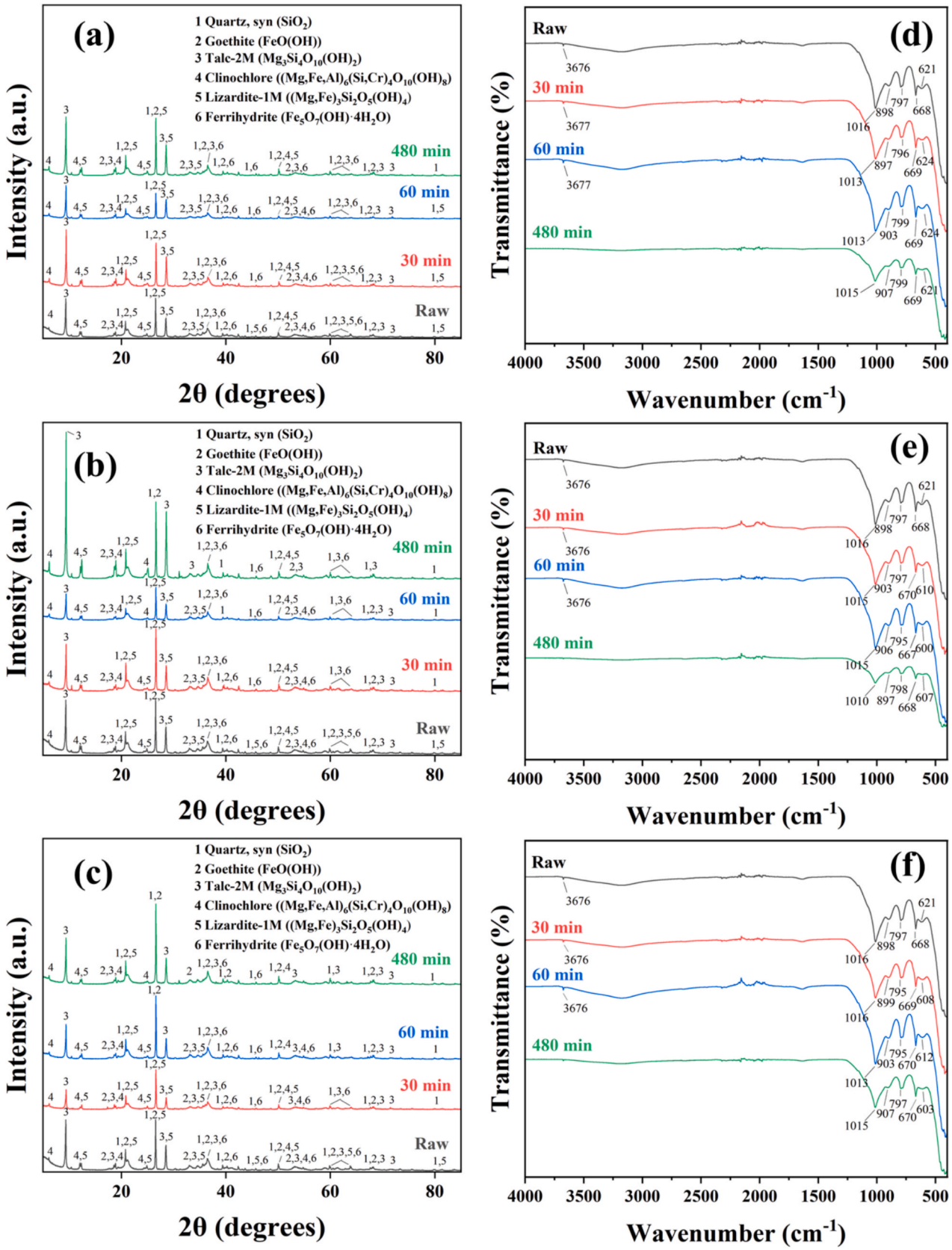

Fig. 5. X-ray diffraction patterns of LL ore leach residues at (a) 25 °C, (b) 45 °C, and (c) 65 °C, and corresponding Fourier-transform infrared spectra at (d) 25 °C, (e) 45 °C, and (f) 65 °C. Leaching times are shown in the legends.

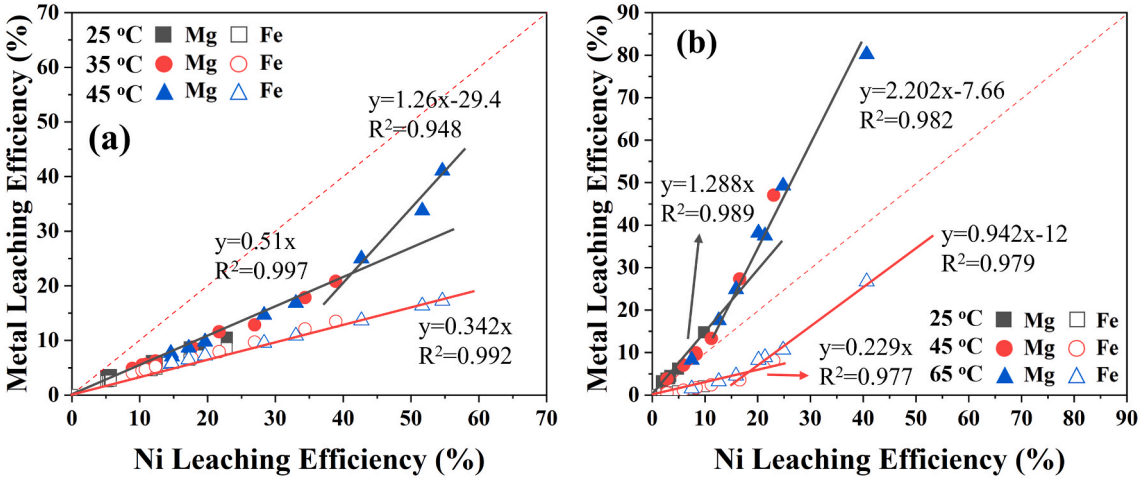

Fig. 6. Correlation in the leaching efficiency between Ni and other metals (Mg and Fe) for (a) SL and (b) LL ores. The red dashed line represents a 1:1 correlation (the leaching efficiencies of Ni and other metals increase proportionally). (For interpretation of the references to colour in this figure legend, the reader is referred to the web version of this article.)

Table 2
Kinetic apparent constants and correlation coefficients from the SC models for SL ore.

Metal	Temperature (°C)	Liquid film diffusion $k_f \times 10^3$ (min^{-1})	R^2	Solid product layer diffusion $k_p \times 10^3$ (min^{-1})	R^2	Chemical reaction $k_r \times 10^3$ (min^{-1})	R^2
Ni	25	4.52	0.873	0.30	0.989	1.62	0.897
	35	7.74	0.876	1.03	0.998	2.94	0.911
	45	11.45	0.848	2.50	0.993	4.70	0.900
Mg	25	2.14	0.798	0.07	0.955	0.74	0.824
	35	4.02	0.881	0.26	0.990	1.43	0.904
	45	7.60	0.939	1.04	0.979	2.90	0.962
Fe	25	1.71	0.844	0.04	0.988	0.59	0.864
	35	2.75	0.829	0.11	0.989	0.95	0.854
	45	11.50	0.848	0.20	0.977	1.29	0.838

Table 3
Kinetic apparent constants and correlation coefficients from the SC models for LL ore.

Metal	Temperature (°C)	Liquid film diffusion $k_f \times 10^3$ (min^{-1})	R^2	Solid product layer diffusion $k_p \times 10^3$ (min^{-1})	R^2	Chemical reaction $k_r \times 10^3$ (min^{-1})	R^2
Ni	25	0.30	0.848	0.007	0.999	0.08	0.851
	45	0.57	0.746	0.04	0.947	0.21	0.764
	65	1.01	0.711	0.15	0.964	0.39	0.752
Mg	25	0.34	0.867	0.02	0.991	0.12	0.878
	45	1.09	0.887	0.20	0.991	0.44	0.920
	65	1.96	0.764	0.80	0.996	0.97	0.872
Fe	25	0.05	0.901	0.0003	0.994	0.016	0.903
	45	0.18	0.926	0.005	0.992	0.06	0.931
	65	0.60	0.911	0.05	0.987	0.22	0.927

3.4.2. *Interpretation of model results*

The fitted kinetic parameters were interpreted to elucidate the temperature-dependent leaching behavior of SL and LL ores. The apparent rate constants increased with temperature for both ores, reflecting the temperature sensitivity of laterite dissolution. The magnitude and pattern of this increase differed distinctly between SL and LL ores. For SL ore, Ni exhibited the highest apparent rate constants under all conditions, which was attributed to its substitution in the T-O structured lizardite. The apparent rate constant of Mg (k_p) increased by approximately 15-fold from 25 °C to 45 °C, indicating that elevated temperature accelerated the structural breakdown of lizardite and enhanced acid accessibility. This pronounced temperature dependence is consistent with the mineralogical changes observed in **Section 3.3.1**. In LL ore, the major mineral phases—clinochlore, talc, and goethite—dissolved at higher temperatures; however, due to their structural stability, the increases in k_p was relatively moderate (approximately 10-fold from 25 °C to 45 °C for Mg).

To further verify the robustness of the SC model-based kinetic interpretation, low-pulp density tests were evaluated under excess-acid conditions using the same kinetic model (Table S6 and S7). The results for both SL and LL ores generally supported solid product layer diffusion control. An exception was observed for Ni and Fe at 65 °C in LL ore, for which the kinetic analysis suggested mixed control; this behavior coincided with a marked increase in Fe leaching efficiency from 27% to 70% under the low-pulp density condition (Fig. S5). This suggests that sufficient acid remains even after Mg-silicate dissolution, allowing additional acid attack to proceed on goethite. Overall, these results demonstrate that pulp density is an important variable governing the co-leaching behavior of Fe and Ni in the LL ore, and further studies are required.

Table 4
Activation energy (E_a) of Ni, Mg, and Fe of SL and LL ores.

Ore type	E_a (kJ/mol) Ni	Mg	Fe
SL ore	82.03	104.83	63.47
LL ore	77.53	55.96	107.19

3.4.3. *Interpretation of activation energies*

Table 4 shows that all metals exhibited the activation energies (E_a) greater than 56 kJ/mol regardless of ore type. This range is substantially higher than the typical values of 4–13 kJ/mol observed in solid product layer diffusion-controlled reactions (Levenspiel, 1998). Because E_a values were derived from Arrhenius plots using three temperature points (df = 1), uncertainty was assessed using 95% confidence intervals (CI) of the regression slope and converted to E_a (Table S8); despite the wide intervals, the E_a values remain within a high range.

This was attributed to product layers that are densely packed or contain materials (SiO_2) with low diffusion coefficients, which hinder the transport of metal ions. Similar behavior has been reported in various hydrometallurgical systems. Gbor et al. reported E_a of 70 and 50

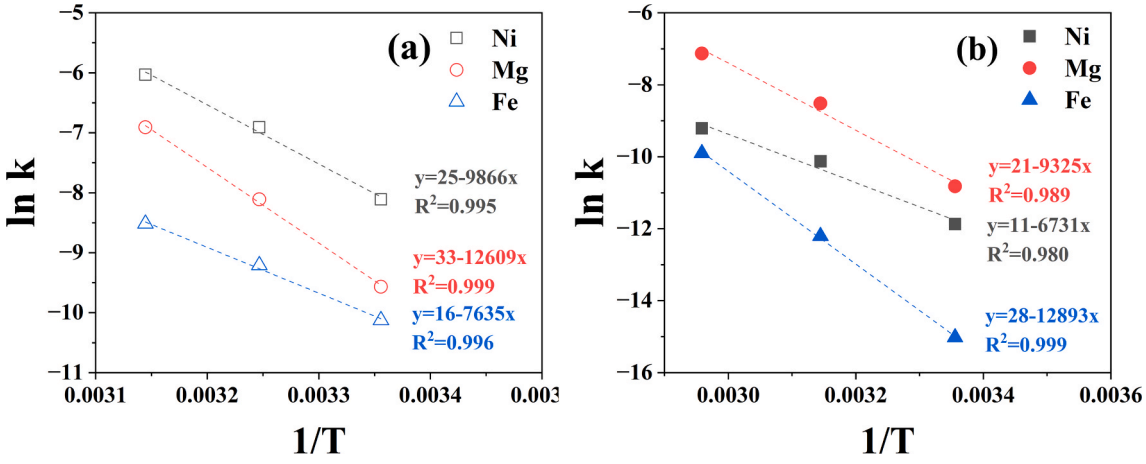

Fig. 7. Relationship between 1/T and ln k of Ni, Mg, and Fe for (a) SL and (b) LL ores.

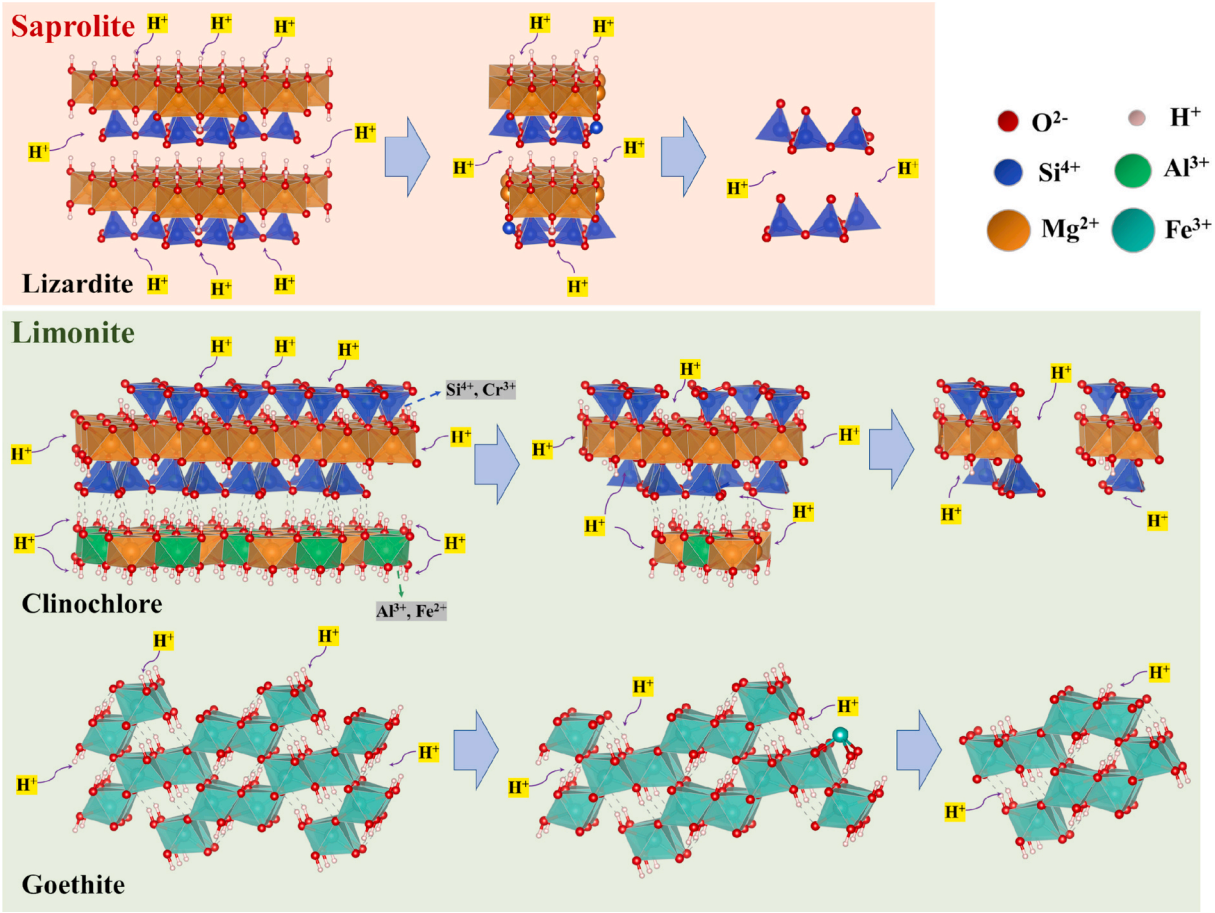

Fig. 8. Schematic diagram of nickel laterite ore leaching behavior.

kJ/mol for Co and Ni, respectively, during nickel slag leaching, despite the reaction being controlled by solid product layer diffusion; these high values were attributed to solid-state diffusion and surface diffusion within the product layer (Gbor et al., 2000). Milićev and Šiftar et al. also observed an activation energy of 109 kJ/mol during $BaSO_4$ dissolution, which they attributed to the compact and diffusion-resistant $BaCO_3$ product layer (Milićev and Šiftar, 1965). Çetintaş and Bingöl et al. further demonstrated that in low-grade laterite leaching, the formation of SiO_2 product layer acted as a diffusion barrier, increasing the E_a of Ni and Fe to 47 and 81 kJ/mol, respectively (Çetintaş and Bingöl, 2016).

Given the limited number of temperature points (df = 1), the CI partially overlap; therefore, metal-to-metal differences in E_a are discussed as qualitative tendencies based on point estimates rather than as statistically strict ordering (Table S8 **and** Fig. 7). In SL ore, E_a generally followed the order of Mg > Ni > Fe, whereas Ni showed the highest leaching efficiency despite its higher E_a compared to Fe (Fig. 2a and c). This discrepancy was attributed to the fact that the leaching efficiency reflects cumulative extraction, but E_a reflects the temperature sensitivity of the apparent reaction rate. Ni is substituted within lizardite and goethite, and its release requires both partial structural breakdown and intra-lattice diffusion, which contributes to its higher E_a compared with Fe. In contrast, the apparent rate constants of Fe showed minimal variation with temperature (Table 2), consistent with its relatively low E_a (Table 4). For LL ore, Ni appeared to exhibit higher E_a than Mg, which was attributed to greater structural constraints associated with Ni in minerals such as clinochlore. Fe exhibited a higher E_a than Ni and Mg, indicating that Fe dissolution is strongly temperature-dependent. This behavior is consistent with Fe being predominantly hosted in structurally stable goethite in LL ore, a phase known to dissolve slowly under atmospheric conditions (Posnjak and Merwin, 1922).

3.5. Schematic summary of laterite ore leaching mechanism

Fig. 8 schematically illustrates the leaching mechanisms of major minerals in SL and LL ores. For SL ore, lizardite is the dominant leachable mineral. Proton attack occurred along the surface and edge of the T-O layers, leading to rapid structural collapse (Sufriadin et al., 2011). In this process, the relatively weak octahedral sheet was destroyed first, the tetrahedral sheet remained, and consequently releasing Ni and Mg. Due to these structural properties, SL ore dissolved fast even at relatively low temperatures. In contrast, in LL ore, the leaching of clinochlore and goethite proceeded gradually with increasing temperature. Clinochlore has a T-O-T structure, and acid attack was restricted to the edge sites (Sufriadin et al., 2011). As a result, its structural breakdown and metal release were slower than in lizardite and showed a stronger temperature dependence. For goethite, protons attacked the surface OH^- groups. This reaction produced H_2O and broke the Fe-O-Fe linkages, thereby releasing Fe ions (Cornell et al., 1976). Thus, the leaching of LL ore proceeded more slowly than that of SL ore, behavior consistent with **Section 3.3**.

4. Conclusions

In this study, leaching experiments were conducted at various temperatures to compare and analyze the atmospheric leaching mechanisms and reaction kinetics of SL and LL ores. The experiments were carried out over relatively short leaching durations, capturing the early stages of metal dissolution. The SL ore showed rapid dissolution at 45 °C, whereas the LL ore required higher temperatures (65 °C) for a significant increase in leaching efficiency. This contrast reflected mineralogical effects, as lizardite in the SL ore readily underwent proton attack and structural collapse, while clinochlore and goethite in the LL ore were more resistant and required higher temperatures to release metals. Kinetic analysis based on the SC models indicated that solid product layer diffusion was the rate-limiting mechanism under all conditions. E_a values from SC model results were all greater than 56 kJ/mol, suggesting a high energy barrier for diffusion. This was attributed to the product layer being composed of silica-rich residues with high diffusion resistance. The early-stage dissolution mechanisms identified in this study can be applied to optimize selective leaching strategies by exploiting the differing temperature sensitivities of SL and LL ores.

5. Supplementary information

The following are provided in the supplementary information: Effect of agitation speed on the leaching efficiencies of Mg, Ni, and Fe for SL and LL ores (Fig. S1), Average acid consumption of SL and LL ores as a function of temperature and time (Table S1), FTIR spectra of leaching residues after washing with deionized water or phosphate buffer solution (Fig. S2), Kinetic apparent constants and correlation coefficients from the SC models for SL (Table S2) and LL ores (Table S3), analyzed separately for the early and late leaching stages, Kinetic analysis plots of Ni, Mg, and Fe using the SC model for SL (Fig. S3) and LL ores (Fig. S4), AIC- and ΔAIC-based model discrimination results for SL (Table S4) and LL ores (Table S5), SC model fitting results for low-pulp density tests for SL (Table S6) and LL ores (Table S7), Leaching efficiencies of Ni, Mg, and Fe under low-pulp density condition (Fig. S5), and 95% confidence intervals of Arrhenius slopes and derived activation energies (Table S8).

CRediT authorship contribution statement

Heewon Kang: Writing – original draft, Investigation, Conceptualization. **Jeongwoo Kim:** Writing – review & editing, Investigation. **Jaehoon Lee:** Writing – review & editing. **Dagyeong Lee:** Investigation. **Daniel Ko:** Writing – review & editing. **Hyunjung Kim:** Writing – review & editing, Supervision, Project administration, Conceptualization.

Declaration of competing interest

The authors declare that they have no known competing financial interests or personal relationships that could have appeared to influence the work reported in this paper.

Acknowledgements

This work was supported by the National Research Foundation of Korea(NRF) grant funded by the Korea government (MSIT) (RS-2024-00406500).

Appendix A. Supplementary data

Supplementary data to this article can be found online at https://doi.org/10.1016/j.mineng.2026.110115

Data availability

Data will be made available on request.

References

Astuti, W., Hirajima, T., Sasaki, K., Okibe, N., 2016. Comparison of atmospheric citric acid leaching kinetics of nickel from different Indonesian saprolitic ores. Hydrometall. 161, 138–151.
Barrón, V., Torrent, J., De Grave, E., 2003. Hydromaghemite, an intermediate in the hydrothermal transformation of 2-line ferrihydrite into hematite. Am. Mineral. 88 (11–12), 1679–1688.
Çetintaş, S., Bingöl, D., 2016. Response surface methodology approach to leaching of nickel laterite and evaluation of different analytical techniques used for the analysis of leached solutions. Anal. Methods 8 (15), 3075–3087.
Chen, C., Gao, J., Yan, Y., 1998. Observation of the type of hydrogen bonds in coal by FTIR. Energy Fuel 12 (3), 446–449.
Cornell, R., Posner, A., Quirk, J., 1976. Kinetics and mechanisms of the acid dissolution of goethite (α-FeOOH). J. Inorg. Nucl. Chem. 38 (3), 563–567.
Ellerbrock, R., Stein, M., Schaller, J., 2022. Comparing amorphous silica, short-range-ordered silicates and silicic acid species by FTIR. Sci. Rep. 12 (1), 11708.

Fan, Q., Yuan, S., Wen, J., He, J., 2024. Review on comprehensive utilization of nickel laterite ore. Miner. Eng. 218, 109044.
Fan, R., Gerson, A.R., 2013. Mineralogical characterisation of Indonesian laterites prior to and post atmospheric leaching. Hydrometall. 134, 102–109.
Faraji, F., Alizadeh, A., Rashchi, F., Mostoufi, N., 2022. Kinetics of leaching: A review. Rev. Chem. Eng. 38 (2), 113–148.
Frost, R.L., López, A., Scholz, R., Wang, L., 2015. A Raman and infrared spectroscopic study of the sulphate mineral aluminite Al2 (SO4)(OH) 4· 7H2O. Spectrochim. Acta A Mol. Biomol. Spectrosc. 148, 232–236.
Ganta, P.B., Morshedizad, M., Kühn, O., Leinweber, P., Ahmed, A.A., 2021. The binding of phosphorus species at goethite: A joint experimental and theoretical study. Minerals 11 (3), 323.
Gbor, P., Ahmed, I., Jia, C., 2000. Behaviour of Co and Ni during aqueous sulphur dioxide leaching of nickel smelter slag. Hydrometall. 57 (1), 13–22.
Gharabaghi, M., Irannajad, M., Azadmehr, A.R., 2013. Leaching kinetics of nickel extraction from hazardous waste by sulphuric acid and optimization dissolution conditions. Chem. Eng. Res. Des. 91 (2), 325–331.
IEA, 2024a. Global EV Outlook 2024. https://www.iea.org/reports/global-ev-outlook-2024.
IEA, 2024b. Renewables 2024. https://www.iea.org/reports/renewables-2024.
Jeong, H.-E., Kang, H., Choi, S., Kim, H., 2025. Comparative study of limonitic and saprolitic laterite ores on the leaching characteristics under atmospheric pressure. Miner. Eng. 226, 109250.
Kamwa, R.A.T., Tome, S., Nemaleu, J.G.D., Noumbissie, L.T., Tommes, B., Eguekeng, I., Spieß, A., Woschko, D., Chongouang, J., Janiak, C., 2023. Effect of curing temperature on properties of compressed lateritic earth bricks stabilized with natural pozzolan-based geopolymer binders synthesized in acidic and alkaline media. Arab. J. Sci. Eng. 48 (12), 16151–16165.
Karppinen, A., Seisko, S., Lundström, M., 2024. Atmospheric leaching of Ni, Co, Cu, and Zn from sulfide tailings using various oxidant. Miner. Eng. 207, 108576.
Khattak, S., Gul, S., Sultana, S., 2023. Synthesis and characterization of nano-silica from locally available laterite clay. Clay Miner. 58 (4), 408–414.
Knittle, E., Phillips, W., Williams, Q., 2001. An infrared and Raman spectroscopic study of gypsum at high pressures. Phys. Chem. Miner. 28 (9), 630–640.
Landers, M., Gilkes, R.J., 2007. Dehydroxylation and dissolution of nickeliferous goethite in New Caledonian lateritic Ni ore. Appl. Clay Sci. 35 (3–4), 162–172.
Levenspiel, O., *Chemical reaction engineering*. 1998, John wiley & sons.
Li, J., Bunney, K., Watling, H., Robinson, D., 2013. Thermal pre-treatment of refractory limonite ores to enhance the extraction of nickel and cobalt under heap leaching conditions. Miner. Eng. 41, 71–78.
Li, J., Xu, Z., Wang, R., Gao, Y., Yang, Y., 2019. Study on leaching kinetics of laterite ore using hydrochloric acid. Physicochem. Probl. Miner. Process. 55.
Liu, P., Zhu, X., Han, Y., Li, Y., Wen, C., 2024. Micropores formation and effects in the magnetization roasting of limonite ore. Powder Technol. 448, 120339.
MacCarthy, J., Nosrati, A., Skinner, W., Addai-Mensah, J., 2016. Atmospheric acid leaching mechanisms and kinetics and rheological studies of a low grade saprolitic nickel laterite ore. Hydrometall. 160, 26–37.
McDonald, R., Whittington, B., 2008. Atmospheric acid leaching of nickel laterites review: Part I. Sulphuric acid technologies. Hydrometallurgy 91 (1–4), 35–55.
Milićev, S., Šiftar, J., Umsetzungen fester Stoffe in Lösungen, 1. Mitt.: Reaktion BaSO4 fest+ K2CO3 gelöst= BaCO3 fest+ K2SO4 gelöst. Monatshefte für Chemie und verwandte Teile anderer Wissenschaften, 1965, 96(3), 941-948.
Mudd, G.M., 2009. Nickel sulfide versus laterite: the hard sustainability challenge remains. In: Proceedings of the 48th Conference of Metallurgists, pp. 23–26.
Mweene, L., Gomez-Flores, A., Jeong, H.-E., Ilyas, S., Kim, H., 2024a. Challenges and future in Ni laterite ore enrichment: A critical review. Miner. Process. Extr. Metall. Rev. 45 (6), 539–563.
Mweene, L., Hong, G., Jeong, H.-E., Kang, H.-W., Kim, H., 2024b. Insights into the changes in the surface properties of goethite with Ni in the lattice in the presence of salicylhydroxamic acid: Experimental and density functional theory studies. Int. J. Miner. Metall. Mater. 31 (4), 665–677.
Norman, R.L., 2014. Incorporation of Nickel Into Synthetic Goethites and the Stabilisation of Mineral Precursor Phases: Implications for Natural Systems. Loughborough University.
Pandey, N., Tripathy, S.K., Patra, S.K., Jha, G., 2023. Recent progress in hydrometallurgical processing of nickel lateritic ore. Trans. Indian Inst. Met. 76 (1), 11–30.
Petrovski, A., Načevski, G., Dimitrov, A., Paunović, P., 2019. Kinetic models of nickel laterite ore leaching process. Machines. Technologies. Materials. 13 (11), 487–490.
Posnjak, E., Merwin, H., 1922. The system, fe2o3—so3—h2o. J. Am. Chem. Soc. 44 (9), 1965–1994.
Rolia, E., Dutrizac, J., 1984. The determination of free acid in zinc processing solutions. Can. Metall. Q. 23 (2), 159–167.
Rubisov, D., Krowinkel, J., Papangelakis, V., 2000. Sulphuric acid pressure leaching of laterites—universal kinetics of nickel dissolution for limonites and limonitic/saprolitic blends. Hydrometall. 58 (1), 1–11.
Saadon, S.A., Yunus, S.M., Yusoff, A.R., Yusop, Z., Azman, S., Uy, D., Syafiuddin, A., 2018. Heated laterite as a low-cost adsorbent for arsenic removal from aqueous solution. Malaysian J. Fundamental Appl. Sci. 14 (1), 1–8.
Srinivasan, T., Rao, P.V., 2014. Free acidity measurement–a review. Talanta 118, 162–171.
Sufriadin, S., Idrus, A., Pramumijoyo, S., Warmada, I.W., Imai, A., 2011. Study on mineralogy and chemistry of the saprolitic nickel ores from Soroako, Sulawesi, Indonesia: Implication for the lateritic ore processing. Journal of Applied Geology 3 (1).
Tabrizi, M.K., Bonalumi, D., Lozza, G.G., 2024. Analyzing the global warming potential of the production and utilization of lithium-ion batteries with nickel-manganese-cobalt cathode chemistries in European Gigafactories. Energy 288, 129622.
Tchio, J.A., Yerima, N., Kaze, C.R., Kamseu, E., Chinje, F.U., Leonelli, C., 2024. Design and characterization of iron–calcium–aluminium–silicate–hydrate as low-temperature binder. Innovative Infrastructure Solutions 9 (2), 42.
Thubakgale, C., Mbaya, R., Kabongo, K., 2013. A study of atmospheric acid leaching of a south african nickel laterite. Miner. Eng. 54, 79–81.
Tian, Q., Dong, B., Guo, X., Xu, Z., Wang, Q., Li, D., Yu, D., 2021. Comparative atmospheric leaching characteristics of scandium in two different types of laterite nickel ore from Indonesia. Miner. Eng. 173, 107212.
Tunç Parlak, T., Yildiz, K., 2024. Investigation of the effect of mechanical activation on nickel and cobalt extraction from laterite at atmospheric pressure by kinetics and leach residue analysis. Can. Metall. Q. 1–18.
Urtnasan, E., Heo, S.-B., Yu, J.-W., Jung, C.-H., Wang, J.-P., 2025. Relationship between Thermodynamic Modeling and Experimental Process for Optimization Ferro-Nickel Smelting. Minerals 15 (2), 101.
von Barsewisch, E.R., Hasty, R.A., 1985. Determination of free acid in the presence of hydrolysable cations by titration. Analyst 110 (10), 1215–1217.
Wanta, K.C., Perdana, I., Petrus, H.T., 2016. Evaluation of shrinking core model in leaching process of Pomalaa nickel laterite using citric acid as leachant at atmospheric conditions. In: IOP Conference Series: Materials Science and Engineering. IOP Publishing.
Wu, Z., Zhang, C., Yuan, F., Lyu, M., Yang, P., Zhang, L., Zhou, M., Wang, L., Zhang, S., Wang, L., 2024. Ni-rich cathode materials for stable high-energy lithium-ion batteries. Nano Energy, 109620.
Zhang, Z.-F., Zhang, W.-B., Zhang, Z.-G., Chen, X.-F., 2024. Nickel extraction from nickel laterites: Processes, resources, environment and cost. China Geology.